Multi-unit rolling isolation system arrays: Analytical model and sensitivity analysis

C. D. Casey[a], P. S. Harvey Jr.[a,*], W. Song[b]

[a]*School of Civil Engineering and Environmental Science, University of Oklahoma, Norman, Oklahoma 73019, USA*
[b]*Department of Civil, Construction and Environmental Engineering, University of Alabama, Tuscaloosa, Alabama 35487, USA*

Abstract

Rolling isolation systems (RISs) have been used extensively to protect vibration-sensitive equipment, such as server cabinets, from earthquake-induced floor motions. These systems are commonly installed in multi-unit arrays to isolate multiple cabinets from harsh floor motions. The mathematical model presented in this paper is an extension of an experimentally-validated model for a single-unit RIS and is amenable to an arbitrary number of isolated cabinets. The proposed model is first compared to free response tests and is then validated with forced response tests using a synthetic waveform representative of earthquake-induced floor motions. An extensive numerical parameter study using the proposed model is carried out to assess the influence of the number of isolated cabinets, as well as mass eccentricity, on the seismic isolation performance of these systems. Through an incremental dynamic analysis it is shown that systems with more cabinets are less prone to impacts, indicating better performance. Rotations produced in the presence of mass eccentricity may induce premature impacts transverse to the loading direction diminishing these systems' performance.

Keywords: rolling isolation, seismic isolation, equipment, floor isolation

1. Introduction

Rolling isolation systems (RISs) have been used extensively to protect structures and nonstructural components from earthquake-induced ground and floor motions. The protected object is mechanically decoupled from horizontal components of ground motions via a rolling interface. Recently, there have been many studies of RISs, with applications ranging from bridges [1–5], to buildings [6–12], to floors

---

Figure 1: Multi-unit rolling isolation system array installation at a financial institution data center. Source: [23].

within a building [13, 14], and to individual objects inside a building [15–21]. RISs are widely used to isolate mission-critical equipment (e.g., server cabinets, mainframes, LAN racks, electronics enclosures, and telecommunications switches) and valuable property. The prediction of the response of equipment isolation systems and their ability to protect building contents requires models that can capture the observed nonlinear behavior of actual RISs subjected to multi-axial loading.

Previous efforts to model RISs have focused on isolating a single cabinet or piece of equipment [18, 22]. However, multiple cabinets commonly need to be protected. Common practice is to install a multi-unit row or *array* of RISs to support and isolate a cluster of cabinets, as shown in Fig. 1. In doing so, additional bearings (beyond the typical four) must be incorporated to support the added load. Because the sub-units are installed in a row, the overall length and aspect ratio of the isolation system change. The displacement across the end bearings due to rotation is proportional to overall length of the RIS, making the multi-unit system more vulnerable to rotations. RISs are known to rotate even in the absence of rotational disturbances due to their chaotic nature and the nonholonomic ball dynamics [18]. These rotations can be exacerbated if the equipment mass is not concentric with the center of stiffness.

In this paper, the equations of motion of multi-unit RIS arrays are derived, incorporating the rolling dynamics of the balls and an arbitrary number of isolated cabinets and mass eccentricity. The resulting mathematical model is used to numerically assess the influence of the number of isolated cabinets and mass eccentricity on the performance of multi-unit RIS arrays subjected to floor motions representative of a range of operating conditions. Isolation performance is characterized by the peak total acceleration experienced by the isolated cabinets, which are compared to a representative threshold for electrical equipment.
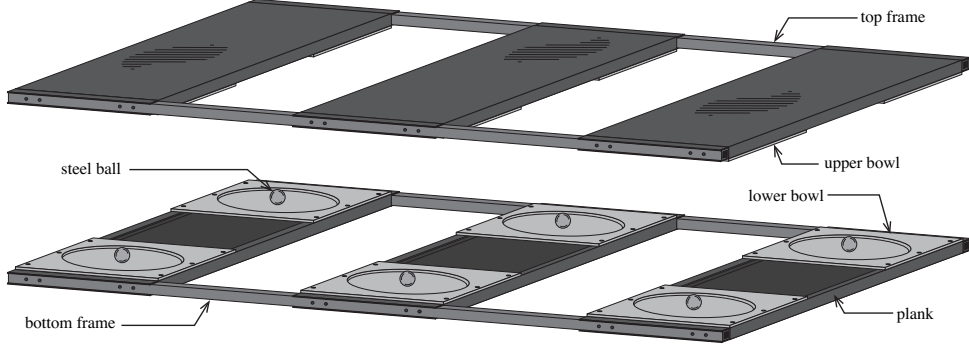
Figure 2: Configuration of an RIS array. The payload mass is carried by the top frame which is supported at various points by steel balls between counter-facing concave bowls. The bottom and top frames isolate groups of equipment from harsh floor motions.

2. Description of the model and modeling assumptions

Consider the multi-unit RIS array illustrated in Figure 2. Vibration-sensitive equipment, such as electrical cabinets, are rigidly connected to the top frame, and the top frame and equipment are mechanically isolated from the bottom frame via *rolling bearings*. Each rolling bearing is composed of a large, steel ball that rolls between a concave-up lower bowl and a concave-down upper bowl. The bearings are configured in pairs on planks that are connected together with steel bars. For a single isolated cabinet, only two planks (four bearings) are required. For N pieces of equipment, $N + 1$ planks are required; e.g., three planks for two cabinets (Figure 2).

2.1. Geometry and notation

Consider the displaced configuration of the RIS illustrated in Figure 3. The bearings are numbered $i = 1, \ldots, n$, where the number of bearings, n, depends on the number of isolated cabinets, N; i.e., $n = 2(N+1)$. The X_t–Y_t coordinates of the ith bowl center are given by $\boldsymbol{\xi}_i = \{x_i, y_i\}_t^{\mathsf{T}},$[1] which is dictated by the frame geometry. The planks are spaced at l_x on centers, with the bearings spaced at l_y on centers.

The N isolated cabinets are assumed to be identical, each having a mass m that is eccentrically located at (e_x, e_y) relative to centroid of the two supporting planks. The total mass of the isolated equipment $M = N \times m$, which is eccentrically located at $\boldsymbol{e} = \{e_x, e_y\}_t^{\mathsf{T}}$ from the top-frame centroid O. The mass moment of inertia about the top-frame centroid is I_O. The top frame undergoes rotation $\theta(t)$ and transla-

---

[1]In this paper, vectors are represented by boldface minuscule letters, and matrices by majuscule letters; the superscript 'T' denotes the transpose; and the subscripts 't' and 'b' are used to indicate the coordinate system in which positions are measured, namely top (X_t, Y_t) and bottom (X_b, Y_b).
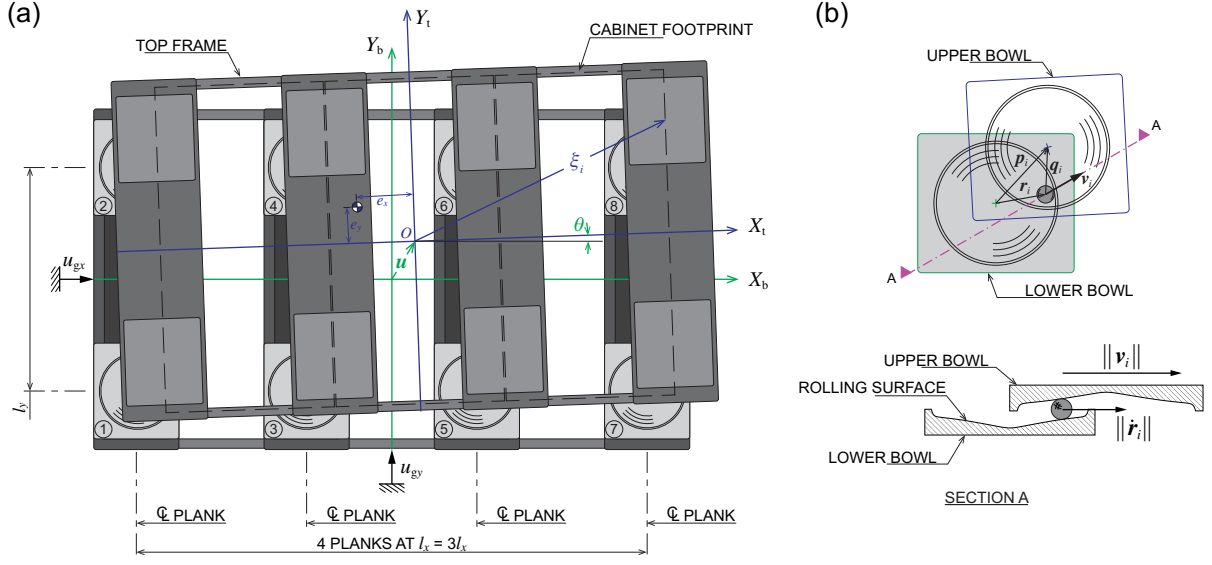
Figure 3: Geometry and notation of a rolling isolation system, $N = 3$: (a) displaced configuration; (b) kinematics of rolling balls.

tional displacement $\boldsymbol{u}(t) = \{u_x(t), u_y(t)\}_{\mathrm{b}}^{\mathsf{T}}$ relative to the bottom frame. The bottom frame is excited by translational disturbance $\boldsymbol{u}_{\mathrm{g}}(t) = \{u_{\mathrm{g}x}(t), u_{\mathrm{g}y}(t)\}_{\mathrm{b}}^{\mathsf{T}}$.

The gravitational restoring forces in the system are attributed to changes in the heights at the bearings, which depend on the top frame's displacement and rotation, as well as the balls' locations. As seen in Fig. 3(b), the balls' locations with respect to the centers of the lower and upper bowls are $\boldsymbol{r}_i(t) = \{r_{xi}(t), r_{yi}(t)\}_{\mathrm{b}}^{\mathsf{T}}$ and $\boldsymbol{q}_i(t) = \{q_{xi}(t), q_{yi}(t)\}_{\mathrm{b}}^{\mathsf{T}}$, and the center-to-center displacement is $\boldsymbol{p}_i(t) = \{p_{xi}(t), p_{yi}(t)\}_{\mathrm{b}}^{\mathsf{T}} \equiv \boldsymbol{u}(t) + (\mathbf{R}_{\theta(t)} - \mathbf{I})\,\boldsymbol{\xi}_i$ where $\mathbf{I}$ is the identity matrix and

$$\mathbf{R}_{\theta(t)} = \begin{bmatrix} \cos\theta(t) & -\sin\theta(t) \\ \sin\theta(t) & \cos\theta(t) \end{bmatrix}$$

All the bowls are assumed axisymmetric with radius-dependent bowl-shape function $\eta(r)$. The height of the top frame at the center of the ith upper bowl is the sum of contributions from the lower and upper bowls, given by

$$h_i \equiv h_i(u_x, u_y, \theta, \boldsymbol{r}_i; t) = \eta(r_i(t)) + \eta(q_i(t)) \tag{1}$$

where $r_i(t) = \|\boldsymbol{r}_i(t)\|$ and $q_i(t) = \|\boldsymbol{q}_i(t)\|$.

2.2. Kinematics of rolling balls

The ball coordinates $r_i(t)$ evolve according to a set of nonholonomic constraints prescribed by the condition of rolling without slipping between non-parallel surfaces [18]. The kinematic constraint, relating the ball velocities $\dot{r}_i(t)$ to the relative velocities of the upper bowls at the ball locations, depends upon the slopes of the upper and lower bowls. For shallow bowls (i.e., small $\eta'(r)$), the nonholonomic constraint can be approximated by the condition that the velocity of the ball center is half of the relative velocity across the isolation system [22]. The ball velocity is in the direction of this relative velocity,

$$\dot{r}_i(t) = \tfrac{1}{2}\left\{\dot{u}(t) + \dot{\theta}(t)\,\mathbf{D}\left[\xi_i + r_i(t) - u(t)\right]\right\}, \qquad (i = 1,...,n) \tag{2}$$

where the cross product $\dot{\theta}\mathbf{k} \times (\xi_i + r_i - u)$ is performed using the matrix

$$\mathbf{D} = \begin{bmatrix} 0 & -1 \\ 1 & 0 \end{bmatrix}$$

The $2n$ non-linear first-order ordinary differential equations (2) prescribe the evolution of the n balls in the X_b–Y_b plane. Initial conditions $r_i(0)$ must be specified.

2.3. Equations of motion

Approaching this problem by using Lagrange's equation, expressions for the kinetic energy $\mathcal{T}$ and potential energy $\mathcal{V}$ need to be found. The kinetic energy $\mathcal{T}$ is given by

$$\mathcal{T}(\dot{u}_x,\dot{u}_y,\theta,\dot{\theta};t) = \tfrac{1}{2}M\mathbf{v}_G^\mathsf{T}\mathbf{v}_G + \tfrac{1}{2}I_G\dot{\theta}^2 \tag{3}$$

in which $\mathbf{v}_G$ is the absolute (horizontal) velocity of the center of gravity G given by

$$\mathbf{v}_G(t) = \dot{u}_g(t) + \dot{u}(t) + \dot{\theta}(t)\mathbf{R}'_{\theta(t)}e \tag{4}$$

where $\mathbf{R}'_\theta = \frac{\partial}{\partial\theta}\mathbf{R}_\theta$, and $I_G = I_O + M(e_x^2 + e_y^2)$. The potential energy $\mathcal{V}$ is due to the change in height of the isolated cabinets' centers of mass. The change in height of a cabinet's center of mass can be interpolated from the heights h_i [Eq. (1)] of the four bowls on the supporting planks [18]. The interpolated height at the center of mass is given by

$$\hat{h}_j = a_1 h_{2j-1} + a_2 h_{2j} + a_3 h_{2j+1} + a_4 h_{2j+2} \tag{5}$$

5

where, in terms of the nondimensional eccentricities $\varepsilon_x = e_x/l_x$ and $\varepsilon_y = e_y/l_y$,

$$\begin{Bmatrix} a_1 \\ a_2 \\ a_3 \\ a_4 \end{Bmatrix} = \frac{1}{4} \begin{bmatrix} 1 & -2 & -2 & 4 \\ 1 & -2 & 2 & -4 \\ 1 & 2 & -2 & -4 \\ 1 & 2 & 2 & 4 \end{bmatrix} \begin{Bmatrix} 1 \\ \varepsilon_x \\ \varepsilon_y \\ \varepsilon_x \varepsilon_y \end{Bmatrix} \tag{6}$$

which is then used to express the potential energy,

$$\mathcal{V}(u_x, u_y, \theta, \boldsymbol{r}_i, \dots, \boldsymbol{r}_n; t) = \sum_{j=1}^{N} mg\hat{h}_j \tag{7}$$

where g is gravitational acceleration. For $N = 1$ (single cabinet) the contribution from the four bearings is the same, but for $N > 1$ (multiple cabinets) the contribution from the bearings on the external planks ($i = 1, 2, n-1, n$) is less than that from the bearings on the interior planks ($i = 3, 4, \dots, n-2$), as the interior planks have twice the tributary area. Eq. (7) can hence be written in the form

$$\mathcal{V} = \sum_{i=1}^{n} mgb_i h_i \tag{8}$$

where the weighting coefficients for the exterior bearings are $b_1 = a_1$, $b_2 = a_2$, $b_{n-1} = a_3$, $b_n = a_4$ and for the interior bearings are

$$b_i = \begin{cases} a_1 + a_3 : & 3 \le i \le n-3, \ i \text{ odd} \\ a_2 + a_4 : & 4 \le i \le n-2, \ i \text{ even} \end{cases}$$

Applying the fundamental nonholonomic form of Lagrange's equation [24, Eq. (2.48)], the equations of motion of the platform coordinates (u_x, u_y, θ), taking into account the constraint (2), are as follows:

$$M\left[\ddot{\boldsymbol{u}}_g(t) + \ddot{\boldsymbol{u}}(t) + \ddot{\theta}(t)\,\mathbf{R}'_{\theta(t)}\boldsymbol{e} - (\dot{\theta}(t))^2\,\mathbf{R}_{\theta(t)}\boldsymbol{e}\right] + \sum_{i=1}^{n} mgb_i\eta'(q_i(t))\,\hat{\boldsymbol{q}}_i(t) + \sum_{i=1}^{n} \tfrac{1}{2}\boldsymbol{\lambda}_i = \mathbf{0} \tag{9a}$$

$$M\left[\ddot{\boldsymbol{u}}_g(t) + \ddot{\boldsymbol{u}}(t)\right]^{\mathsf{T}}\mathbf{R}'_{\theta(t)}\boldsymbol{e} + I_O\,\ddot{\theta}(t) + \sum_{i=1}^{n} mgb_i\eta'(q_i(t))\hat{\boldsymbol{q}}_i^{\mathsf{T}}(t)\mathbf{R}'_{\theta(t)}\boldsymbol{\xi}_i$$
$$+ \sum_{i=1}^{n} \tfrac{1}{2}\boldsymbol{\lambda}_i^{\mathsf{T}}\mathbf{D}[\boldsymbol{\xi}_i + \boldsymbol{r}_i(t) - \boldsymbol{u}(t)] = 0 \tag{9b}$$

where $\boldsymbol{q}_i(t) = \boldsymbol{p}_i(t) - \boldsymbol{r}_i(t)$, as in Figure 3; the over-hat indicates the unit vector, e.g., $\hat{\boldsymbol{r}}_i \equiv \boldsymbol{r}_i/\|\boldsymbol{r}_i\|$; and $\boldsymbol{\lambda}_i$ are the Lagrange multipliers enforcing Eq. (2). The multipliers are found by applying Lagrange's equation

to the ball coordinates $\boldsymbol{r}_i$:

$$\lambda_i = \mathbf{f}_i^{\mathrm{d}} + mgb_i \left[\eta'(r_i(t)) \, \hat{\boldsymbol{r}}_i(t) - \eta'(q_i(t)) \, \hat{\boldsymbol{q}}_i(t) \right] \tag{10}$$

where the damping forces $\mathbf{f}_i^{\mathrm{d}}$ counteract the balls' motion. The form of $\mathbf{f}_i^{\mathrm{d}}$ depends on the ball–bowl interface, which can range from lightly damped (steel-on-steel [18]) to heavily damped (rubber coated balls [19] or rubber coated bowls [22, 25–27]). Substituting Eq. (10) into Eq. (9) and combining terms,[2] the equations of motion of the platform coordinates can be rewritten in matrix form:

$$
\begin{bmatrix} M\mathbf{I} & M\mathbf{D}\mathbf{R}_{\theta(t)}\boldsymbol{e} \\ M(\mathbf{D}\mathbf{R}_{\theta(t)}\boldsymbol{e})^{\mathsf{T}} & I_O \end{bmatrix} \begin{Bmatrix} \ddot{\boldsymbol{u}}(t) \\ \ddot{\theta}(t) \end{Bmatrix} + \begin{Bmatrix} -M(\dot{\theta}(t))^2 \, \mathbf{R}_{\theta(t)}\boldsymbol{e} \\ 0 \end{Bmatrix}
$$

$$
+ \frac{1}{2} \sum_{i=1}^{n} \begin{bmatrix} \mathbf{I} \\ (\boldsymbol{\xi}_i + \boldsymbol{r}_i(t) - \boldsymbol{u}(t))^{\mathsf{T}}\mathbf{D}^{\mathsf{T}} \end{bmatrix} \left(\mathbf{f}_i^{\mathrm{d}} + \mathbf{f}_i^{\mathrm{L}} + \mathbf{f}_i^{\mathrm{U}} \right) = - \begin{bmatrix} M\mathbf{I} \\ M(\mathbf{D}\mathbf{R}_{\theta(t)}\boldsymbol{e})^{\mathsf{T}} \end{bmatrix} \ddot{\boldsymbol{u}}_{\mathrm{g}}(t) \tag{11}
$$

where the lower and upper gravitational restoring forces are defined respectively by

$$\mathbf{f}_i^{\mathrm{L}} = mgb_i \eta'(r_i(t)) \, \hat{\boldsymbol{r}}_i(t) \tag{12a}$$

$$\mathbf{f}_i^{\mathrm{U}} = mgb_i \eta'(q_i(t)) \, \hat{\boldsymbol{q}}_i(t) \tag{12b}$$

Eqs. (2) and (11) comprise the full set of system dynamics, which must be integrated simultaneously. The equations of motion for the platform coordinates [Eq. (11)] represent an extension of a previously developed model that was valid only for the case of $N = 1$ ($n = 4$) [18, 22] to be able to accommodate an arbitrary number of isolated cabinets ($N > 1$). Upon closer inspection, Eq. (11) reduces to those previous models if N is taken to be 1.

2.4. Typical bowl geometry and damping model

The mathematical model [Eq. (11)] requires the bowl-shape function $\eta(r)$ and the damping model to be specified. A typical bowl-shape function $\eta(r)$ is conical with a spherical central region and lip at the edge [21, 28]. For this shape, the bowl gradient, which appears in the gravitational restoring forces [Eq. (12)], is

---

[2]Note that $\mathbf{R}_\theta' \equiv \mathbf{D}\mathbf{R}_\theta$, $\mathbf{R}_\theta \boldsymbol{\xi}_i \equiv \boldsymbol{\xi}_i + \boldsymbol{r}_i - \boldsymbol{u} - \boldsymbol{q}_i$, and $\hat{\boldsymbol{q}}_i^{\mathsf{T}} \mathbf{D} \boldsymbol{q}_i \equiv 0$.

given by

$$\eta'(r) = \begin{cases} \dfrac{r}{\sqrt{R^2 - r^2}}, & r \leq R\sin[\arctan(s)] \\ s, & R\sin[\arctan(s)] < r \leq r_o \\ s_o(r - r_o) + s, & r > r_o \end{cases} \tag{13}$$

where r is the location of the ball relative to the center of the bowl, R is the radius of curvature in the spherical region in the center of the bowl, s is the slope of the conical section of the bowl, r_o is the radial distance to the bowl lip/edge, and s_o is the slope to represent impact with the lip. Note that this model assumes a linear Hooke impact model, as opposed to a nonlinear impact model such as the Hertz model [29].

Commonly, the bowls and balls are both made of stainless steel, i.e., *lightly damped*, which is considered here. For a lightly damped RIS, linear viscous damping is appropriate: $\mathbf{f}_i^d = c_i \mathbf{r}_i$ where c_i is the mass-dependent damping coefficient [18]. The damping coefficient c_i depends on the normal force carried by each ball. Values for the damping coefficients were fitted to experimental data of lightly damped RISs in a previous study [18, Eq. (51)], which considered a single cabinet configuration ($N = 1$) with no mass eccentricity (i.e., with each ball carrying one fourth the mass m). The largest mass considered in that study was only 635 kg. To account for larger masses and mass eccentricity, the following relationship is proposed

$$c_i = \begin{cases} 0.000229(4m_i)^2 + 0.02884(4m_i), & m_i \leq 160 \text{ kg} \\ 1.288m_i - 93.80, & m_i > 160 \text{ kg} \end{cases} \tag{14}$$

where $m_i = mb_i$ is the mass allocated to the ith bearing. The first equation is simply the fitted values from Ref. [18] over the applicable range of masses; the 4 accounts for the equal mass distribution in the absence of mass eccentricity (i.e., $b_i = 1/4$, $i = 1, 2, 3, 4$). The second equation is a linear extrapolation from $m_i = 160$ kg to higher masses not tested in Ref. [18]. It is important to note that a linear viscous damping model is not valid for rolling bearings with supplemental damping (e.g., rolling surfaces coated with an elastomeric material [30]), which would require a more sophisticated rolling resistance model [31, 32].

3. Experimental calibration and validation

The mathematical model developed in the preceding section is used to assess the performance of multi-unit RIS arrays under parametric variation in Section 4. The isolated cabinet and RIS geometries considered
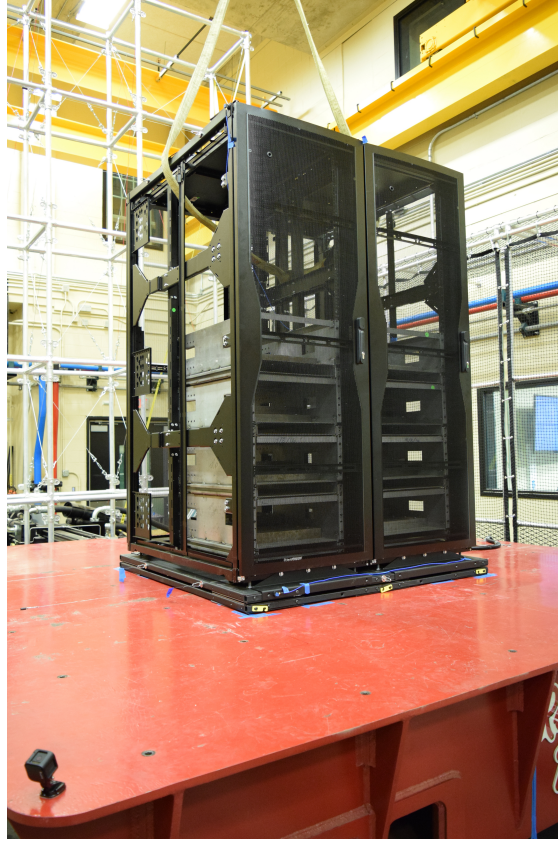
Figure 4: Picture of the experimental setup: ganged ($N = 2$) cabinet configuration in the front-to-back orientation.

in the numerical simulations are described below. These geometries are representative of a typical installation that would be seen in the field and correspond to actual network cabinets and RISs previously tested in the lab [33]. The experimental setup is shown in Fig. 4. The experimental setup was instrumented with an array of sensors to measure the displacements and accelerations of the shake table and the isolation system. The table's displacement and acceleration were measured with an LVDT and a uniaxial accelerometer, respectively. The orthogonal displacements and rotation of the isolation system were measured with three string potentiometers connected to the top frame (just above the isolation layer) and attached to a fixed reference frame. Two triaxial accelerometers located at opposite corners of the top frame of the isolation system to measure the total accelerations at the base of the isolated cabinet. See Ref. [33] for additional details on the experimental setup and testing program. The model incorporating the experimental operating conditions is first calibrated to free response tests and then validated with forced response tests.

The mathematical model is implemented into MATLAB (Mathworks, Natick, MA), and the complete set of equations that describe the evolution of the system [Eqs. (2) and (11)] are solved simultaneously using the
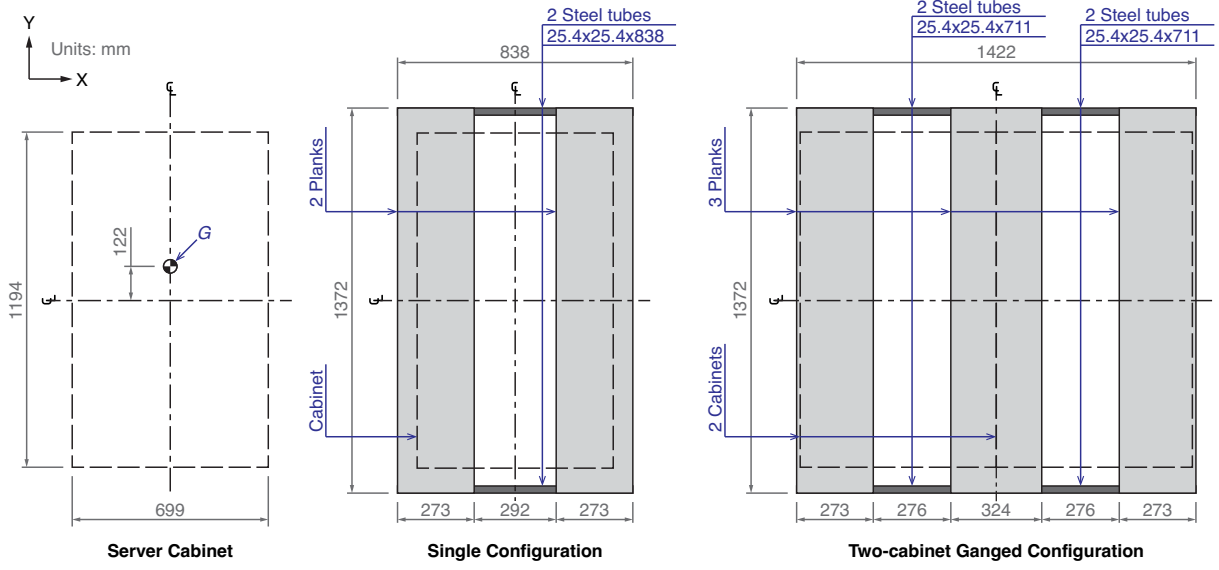
9

Figure 5: Plan dimensions of server cabinet and single ($N = 1$) and ganged ($N = 2$) cabinet configurations.

ode45 solver in MATLAB, which requires the equations of motion in state-space form: $\dot{\mathbf{x}}(t) = \mathbf{f}(\mathbf{x}, \ddot{u}_{gx}, \ddot{u}_{gy}; t)$ where the inputs are the ground accelerations $\ddot{u}_{gx}(t)$ and $\ddot{u}_{gy}(t)$. The states of the system are the platform translational and rotational displacements and velocities and the ball translational displacements:

$$\mathbf{x}(t) = \begin{bmatrix} u_x(t) & u_y(t) & \theta(t) & \dot{u}_x(t) & \dot{u}_y(t) & \dot{\theta}(t) & r_{1x}(t) & r_{1y}(t) & \cdots & r_{nx}(t) & r_{ny}(t) \end{bmatrix}^{\mathsf{T}} \in \mathbb{R}^{6+2n} \tag{15}$$

The states are initialized to zero for all cases, i.e., $\mathbf{x}(0) = \mathbf{0}$. The ode45 solver uses a 4th-order Runge-Kutta method with an adaptive time step. Tight error tolerances, both relative and absolute, were used to ensure numerical accuracy.

3.1. Considered setup and properties

The dimensions ($H \times D \times W$) of each isolated network cabinet are 2026-mm $\times$ 1194-mm $\times$ 699-mm (see Fig. 5), with a mass m of 705 kg. The center of mass (G) of the experimental cabinets was 740 mm from the base, concentric about the width ($e_x = 0$), and 122 mm forward-of-center in the cabinet depth ($e_y = 122$ mm). Other values of e_y will be considered in Section 4.

Determination of I_O must consider how the cabinet mass is distributed, as well as the spacing of the cabinets and their position relative to the top-frame centroid O. To be consistent with the development of the potential energy [Eq. (8)], an individual cabinet mass m is allocated to the centers of each supporting bearing with each cabinet contributing ma_i, where a_i is given by Eq. (6). The total mass contributed to a

10

given bearing located at $\boldsymbol{\xi}_i$ is $m_i = mb_i$ $(i = 1,...,n)$. Treating the allocated masses as point masses, the mass moment of inertia about the centroid O is given by

$$I_O = \sum_{i=1}^{n} m_i \boldsymbol{\xi}_i^{\mathsf{T}} \boldsymbol{\xi}_i \tag{16}$$

Two configurations were experimentally tested: single cabinet ($N = 1$) and two ganged cabinets ($N = 2$). In both cases, the bearing spacing, as denoted in Fig. 3(a), are taken to be $l_x = 57$ cm and $l_y = 110$ cm (see Figure 5). For the eccentricity $(e_x, e_y) = (0, 122$ mm), $a_1 = a_3 = 0.19$ and $a_2 = a_4 = 0.31$. So, for the single cabinet setup, $m_1 = m_3 = 137$ kg, $m_2 = m_4 = 215$ kg, and $I_O = 270$ kg m^2. For the two-cabinet ganged setup, the bearings on the middle plank carry twice the mass ($m_3 = 273$ kg and $m_4 = 431$ kg), and $I_O = 656$ kg m^2. These allocated masses are used to determine the damping coefficients c_i from Eq. (14).

The gravitational restoring forces given by Eq. (12) depend explicitly on the bowl gradient $\eta'(r)$. The form of the gradient is taken to be Eq. (13), where nominal values for R, s, and r_o are 12.7 cm, 0.1, and 9 cm, respectively [21]. The nominal radius $R = 12.7$ cm gave good agreement with the acceleration-displacement at small displacements. The peak acceleration in the horizontal direction over the conical section of the rolling surface is governed by the slope s and is approximately $0.1g$ [34]. However, after initial numerical trials, the stiffness was found to be high, and therefore the periods of the numerical results were lower than that of the experimental trials. The slope of the conical section of the bowl was modified in order to match the periods of the systems; a slope of 0.095 provided good agreement with the period of the experimental results. At a ball displacement $r > 9$ cm, impact occurs with the lip/edge of the bowl. In order to simulate the impact, a high stiffness is used. A value of $s_o = 100$ produced the acceleration spikes needed for impact, but also preserved model stability for grazing impacts of the lip/edge.

3.2. Free response results

The mathematical model for a multi-unit RIS array with $N = 1$ and 2 cabinets was first compared to experimental free response tests. Experimental free response was achieved by exciting the RIS and cabinets with an abrupt motion from the shake table in the Y direction (see Fig. 3) with a velocity of 75 cm/s and a total displacement of 15 cm. The longitudinal and transverse displacements (u_y, u_x) and rotation (θ) were measured along with the longitudinal and transverse total accelerations. Fig. 6 shows the response for the ganged cabinet setup. Excellent agreement is seen between the experimental results and the numerical prediction. Similar results were found for the single cabinet setup (not shown). The
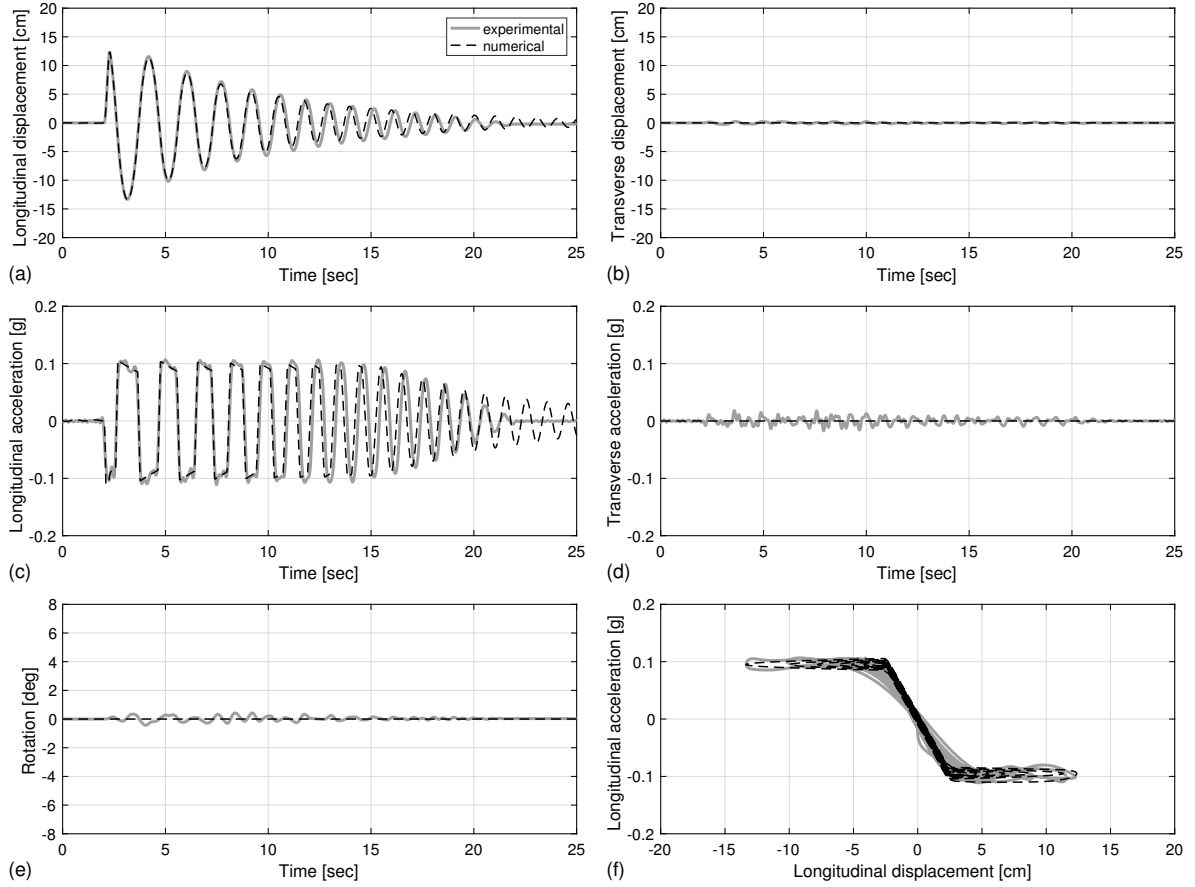
11

Figure 6: Experimental and numerical free response results for ganged cabinets ($N = 2$) with bare steel dishes in the front-to-back orientation: (a) longitudinal displacement, $u_y(t)$; (b) transverse displacement, $u_x(t)$; (c) longitudinal acceleration, $\ddot{u}_y(t) + \ddot{u}_{gy}(t)$; (d) transverse acceleration, $\ddot{u}_x(t) + \ddot{u}_{gx}(t)$; (e) rotation, $\theta(t)$; and (f) longitudinal acceleration versus longitudinal displacement.

numerical results for the single cabinet showed good agreement over the first five cycles of motion, after which the experimental system began to respond in the transverse direction with rotation. Due to slight asymmetries in the experimental system, energy in the longitudinal direction transitioned into the transverse and rotational modes. The numerical model however is perfectly symmetrical in the Y (front-to-back) direction, so transverse displacements and rotations are not predicted. The numerical results for the ganged cabinets (Fig. 6) shows good agreement with the experimental for the entirety of the test as very little of the longitudinal energy transitioned into the transverse and rotational modes.

3.3. Forced response results

Next, the mathematical model was validated against forced response tests. The inputs to the mathematical model are the ground-motion accelerations $\ddot{u}_{gx}(t)$ and $\ddot{u}_{gy}(t)$. A uniaxial ground motion $\ddot{u}_g(t)$ is
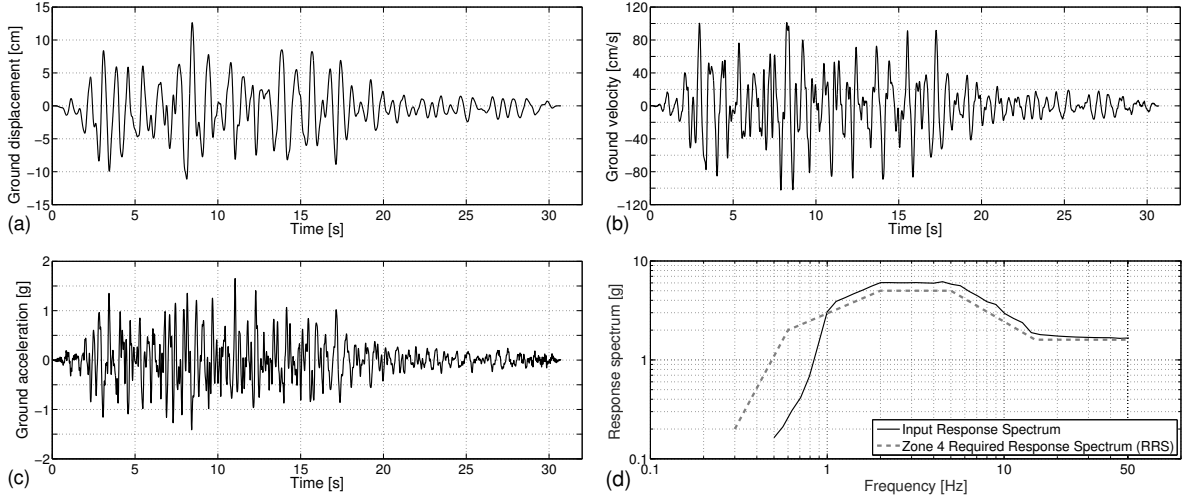
Figure 7: Ground motion waveform — (a) displacement $u_\mathrm{g}(t)$ (b) velocity $\dot{u}_\mathrm{g}(t)$, and (c) acceleration $\ddot{u}_\mathrm{g}(t)$ — and (d) 2%-damped response spectrum.

considered, and the angle of incidence α is varied; i.e., $\ddot{u}_{\mathrm{g}x}(t) = \ddot{u}_\mathrm{g}(t)\cos\alpha$ and $\ddot{u}_{\mathrm{g}y}(t) = \ddot{u}_\mathrm{g}(t)\sin\alpha$. The uniaxial ground motion $\ddot{u}_\mathrm{g}(t)$ used for this study is the Zone-4 VERTEQ-II record shown in Fig. 7. This is a synthetically generated record with a broadband frequency spectrum. The record was synthesized from several typical earthquakes and for different building and site soil conditions. It is spectrally compatible with the floor acceleration of a building located in a high seismic zone. VERTEQ-II was originally developed for testing of telecommunications equipment [35], making it an appropriate waveform for this study.

Angles of incidence of 0 and 90° are considered, which represent loading in the *side-to-side* (X) and *front-to-back* (Y) directions, respectively. Four different configurations were experimentally tested and used for the model validation: the single cabinet and the double cabinet each loaded in both directions. Figs. 8 and 9 show the time histories of the experimental and numerical results for the ganged cabinet setups loaded in the front-to-back direction at ground-motion (GM) scaling of 75 and 100%, respectively. Fig. 10 shows the results for the ganged cabinet setups loaded in the side-to-side direction at a ground-motion (GM) scaling of 100%.

At 75% GM scaling in the front-to-back direction (Fig. 8), the model shows excellent agreement with the experimental results, predicting the response nearly perfectly up until impact at 8 s [indicated by the dots in Fig. 8(a)]. At the point of impact, a large spike in the acceleration is observed and predicted. Prior to impact, the experimental system exhibits rotations up nearly 4° (Fig. 8(e)), which are not predicted by the model due to the perfect symmetry assumed in the model as previously discussed.
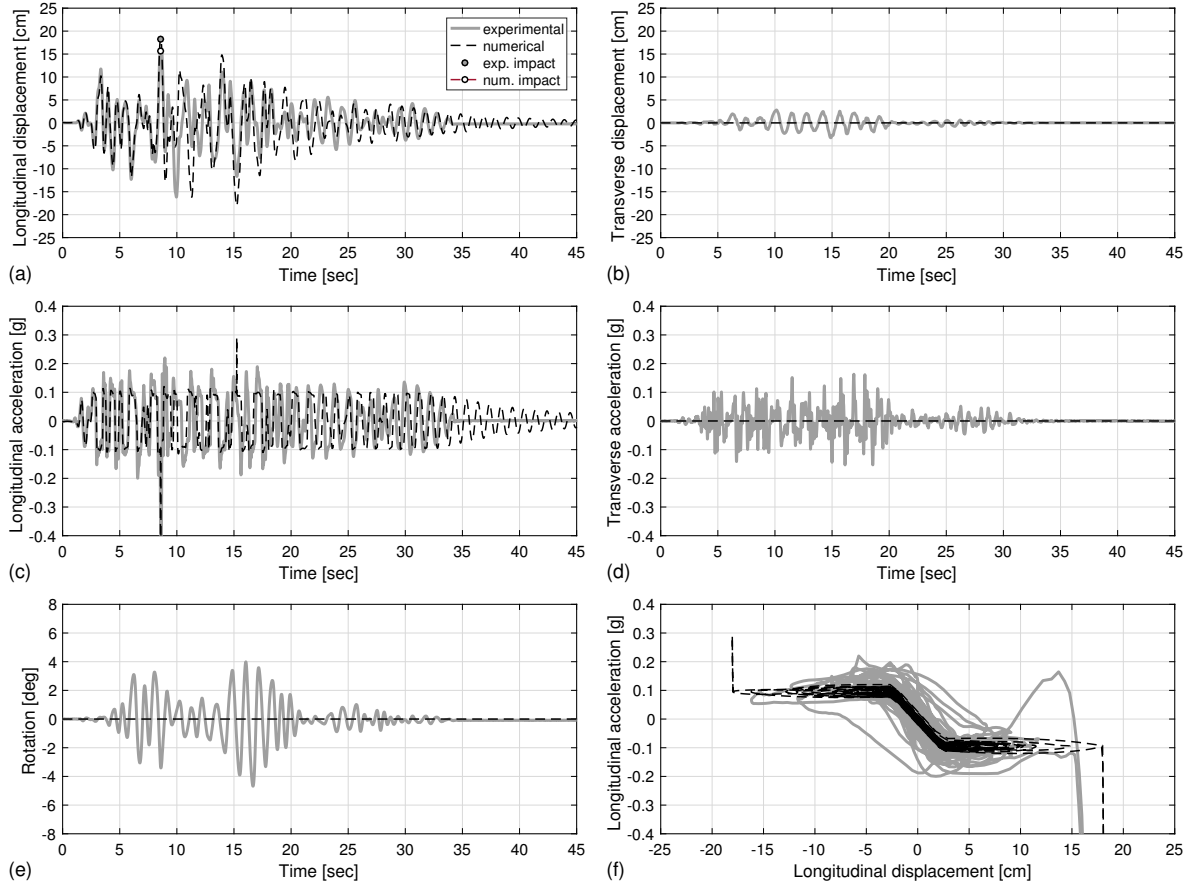
13

Figure 8: Experimental and numerical forced response results at 75% GM scaling for ganged cabinets ($N = 2$) with bare steel dishes in the front-to-back orientation: (a) longitudinal displacement, $u_y(t)$; (b) transverse displacement, $u_x(t)$; (c) longitudinal acceleration, $\ddot{u}_y(t) + \ddot{u}_{gy}(t)$; (d) transverse acceleration, $\ddot{u}_x(t) + \ddot{u}_{gx}(t)$; (e) rotation, $\theta(t)$; and (f) longitudinal acceleration versus longitudinal displacement.

At 100% GM scaling in the front-to-back direction (Fig. 9), again good agreement is observed, predicting peak responses and phasing, up until the point of impact. However, in this case, the time of impact is not predicted correctly. The experimental response exhibits a light impact at 10 s, as seen by the small spike in longitudinal acceleration ($0.24g$). Before this impact the rotations are relatively small ($< 1°$), but increase to $4°$ following the impact. As a result, there is a subsequent impact at 15 s. This impact is not captured by the numerical model, but a later impact at about 18 s is predicted. The results for the numerical model after impact are not shown as they are suspect because the model does not account for the energy loss of the impact and produces high restoring forces due to the elastic action of the stiffness which acts at the edge/lip of the bowl [see Eq. (13)]. In actuality, these forces are not elastic and would not behave as seen in the model. However, the purpose of the model is to capture if/when impacts occur, as opposed to
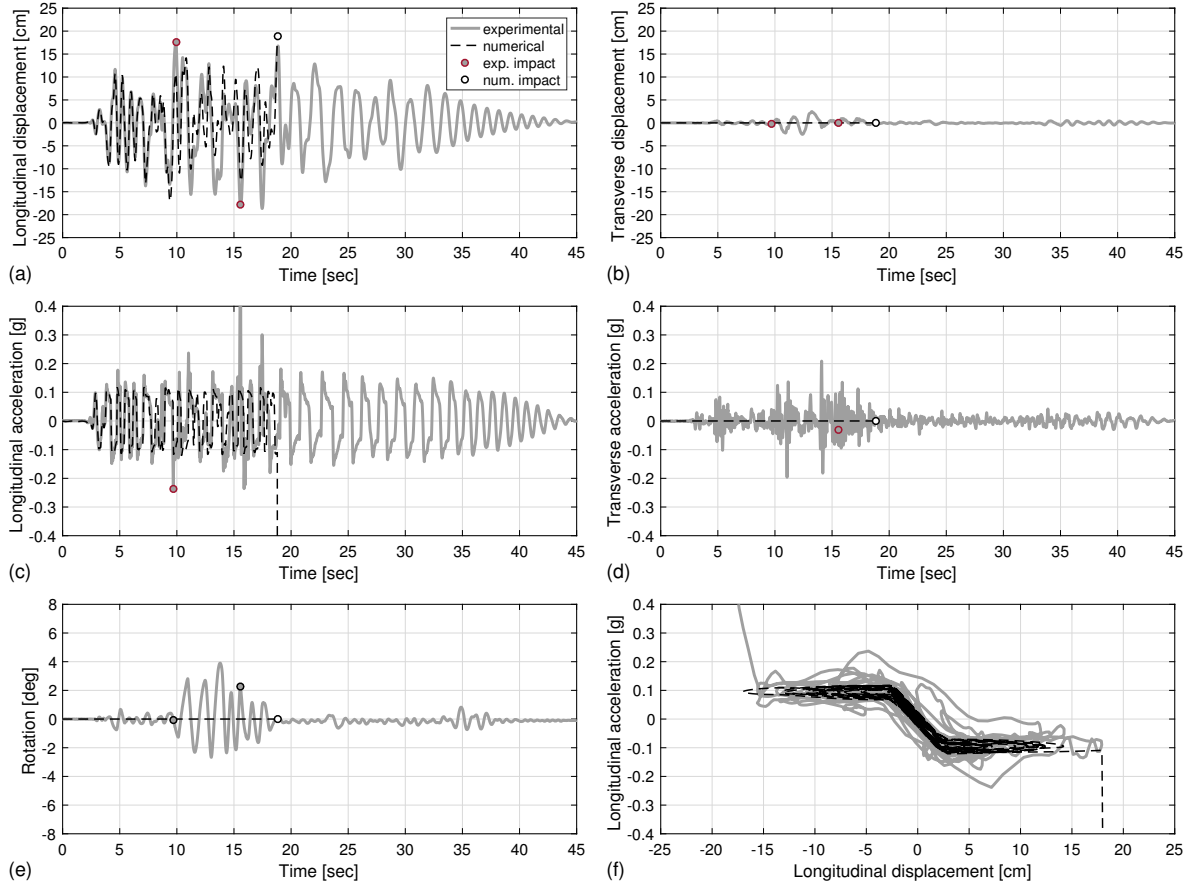
Figure 9: Experimental and numerical forced response results at 100% GM scaling for ganged cabinets ($N = 2$) with bare steel dishes in the front-to-back orientation: (a) longitudinal displacement, $u_y(t)$; (b) transverse displacement, $u_x(t)$; (c) longitudinal acceleration, $\ddot{u}_y(t) + \ddot{u}_{gy}(t)$; (d) transverse acceleration, $\ddot{u}_x(t) + \ddot{u}_{gx}(t)$; (e) rotation, $\theta(t)$; and (f) longitudinal acceleration versus longitudinal displacement.

the exact value of the high accelerations sustained at impact.

At 100% GM scaling in the side-to-side direction (Fig. 10), the model predicts an impact at 8 s, which is attributed to large longitudinal displacements (16 cm) compounded with appreciable rotation (2°). Rotations are predicted by the model (Fig. 10(e)) for this case because of the mass eccentricity in the side-to-side direction. While rotations develop experimentally, they do not lead to impacts at the time predicted, but instead subsequently at 17 s.

In summary, the model does a good job predicted displacements, accelerations, and rotations initially, but due to the chaotic nature of these systems [18] the trajectories diverge following impacts or after a few cycles of motion. The divergence can be attributed to slight imperfections in the experimental system that are not captured by the model. These imperfections lead to rotations in the experimental system even when
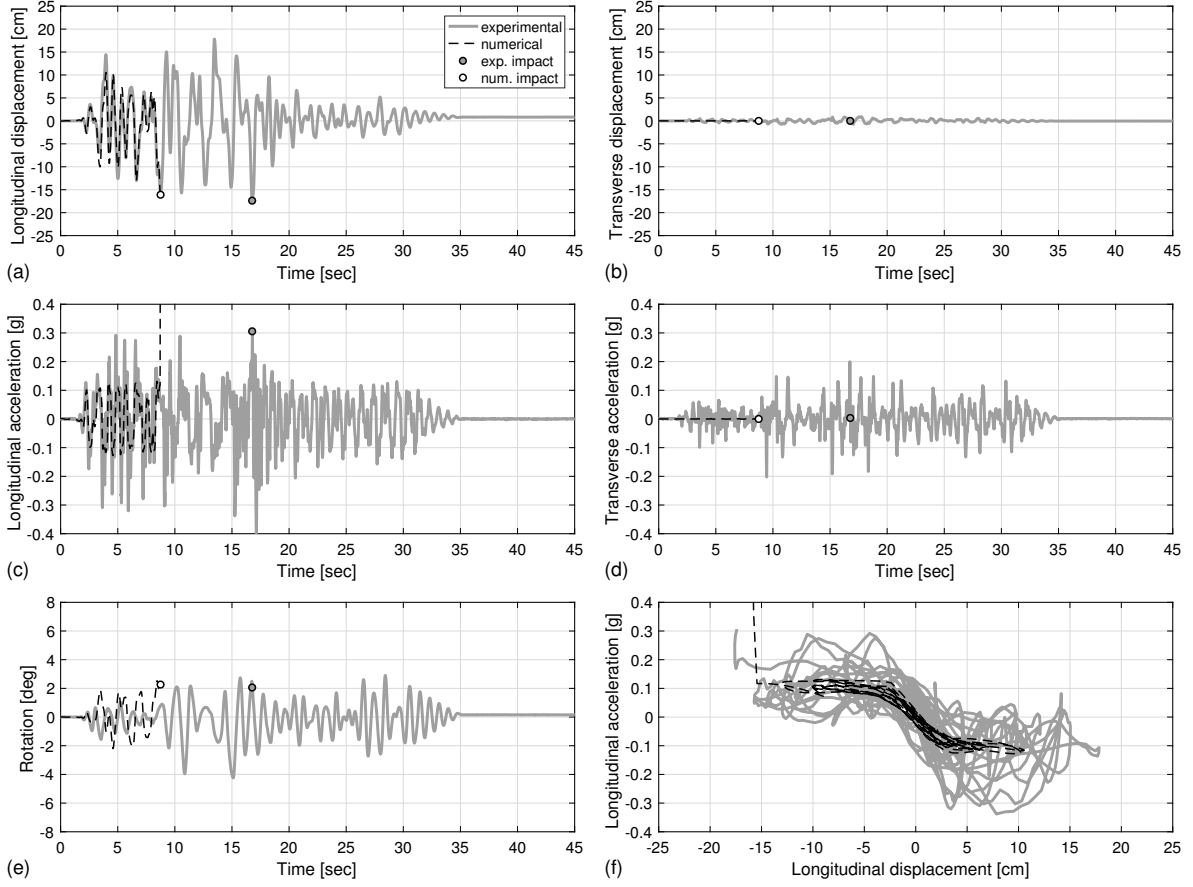
Figure 10: Experimental and numerical forced response results at 100% GM scaling for ganged cabinets ($N = 2$) with bare steel dishes in the side-to-side orientation: (a) longitudinal displacement, $u_x(t)$; (b) transverse displacement, $u_y(t)$; (c) longitudinal acceleration, $\ddot{u}_x(t) + \ddot{u}_{gx}(t)$; (d) transverse acceleration, $\ddot{u}_y(t) + \ddot{u}_{gy}(t)$; (e) rotation, $\theta(t)$; and (f) longitudinal acceleration versus longitudinal displacement.

the system is loaded front-to-back (i.e., without mass eccentricity). Transverse displacements (Figs. 8(b), 9(b), and 10(b)) and accelerations (Figs. 8(d), 9(d), and 10(d)) are also experimentally observed, but are not predicted by the model. Nonetheless, while the model does not always predict the correct instance in time at which impact occurs, it successfully predicts the occurrence of an impact, which is satisfactory for this study focused on sensitivity to number of cabinets (N) and mass eccentricity (e_y).

4. Incremental dynamic analysis

In order to evaluate which RIS configurations result in lower risk of failure, incremental dynamic analysis (IDA) is conducted. IDA curves for isolated cabinets with different numbers of ganged cabinets and different mass eccentricities are presented in Sections 4.2 – 4.4. Single ($N = 1$) and ganged ($N = 2, 4$,
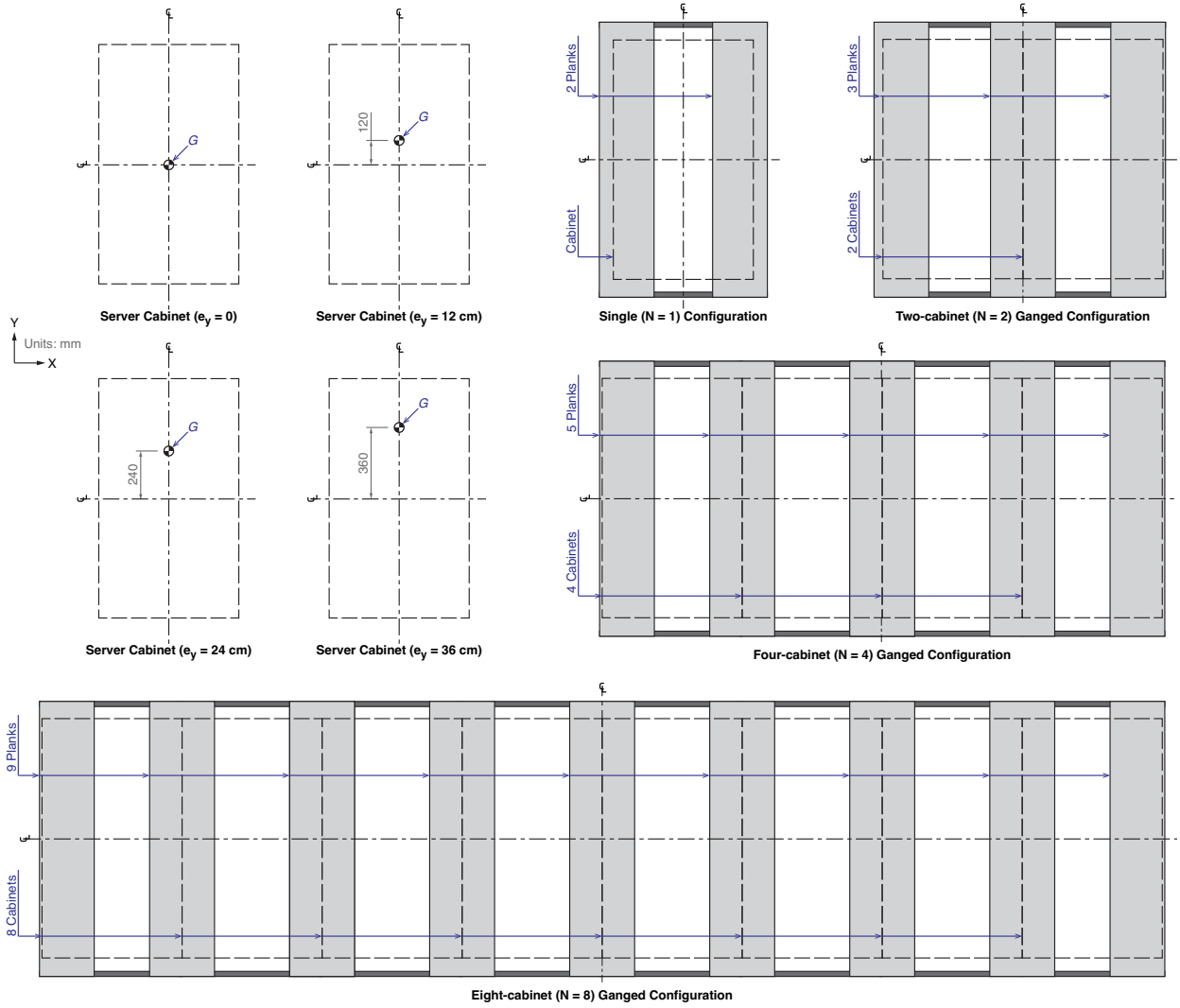
16

Figure 11: Schematic of the geometrical configurations considered in the incremental dynamic analysis: Server cabinets with eccentricity $e_y = 0$, 12, 24, and 26 cm, in arrays of $N = 1$ (single), 2, 4 and 8 ganged configurations.

and 8[3]) cabinet configurations are considered, and the mass eccentricity e_y is varied from 0 to 36 cm at increments of 12 cm, while fixing $e_x = 0$.

The Zone-4 VERTEQ-II waveform (Fig. 7) is used, and the motion is scaled from 0 to 100% at increments of 5%; the ground-motion (GM) scaling serves as the intensity measure. Two loading directions are considered: 0° (side-to-side) and 90° (front-to-back). Due to the location of the center of mass (i.e., along the centerline of the cabinet), the front-to-back orientation is identical to the side-to-side orientation with

---

[3]For more than 8 isolated cabinets, ganged rolling isolation systems are impractical, and an isolated raised floor would be better suited [36].

$e_y = 0$; therefore, the results for the front-to-back orientation are not shown, but may be interpreted from the side-to-side case with $e_y = 0$. The engineering demand parameters of interest are intrinsically linked to the failure modes of the electrical cabinets, which are described here.

4.1. Engineering demand parameters

Vibration-sensitive equipment such as electrical cabinets are typically rated according to peak accelerations they can sustain and remain operational. For example, IBM suggests operational vibration limits of $0.1g$ and $0.3g$ peak acceleration for light and heavy floor mounted machines in an office environment [37]. Hence, the first engineering demand parameter is the peak total acceleration sustained by the isolated equipment. The total acceleration at the centroid of each cabinet is calculated as follows:

$$\boldsymbol{a}_j^t(t) = \ddot{\boldsymbol{u}}_g(t) + \ddot{\boldsymbol{u}}(t) + \ddot{\theta}(t)\mathbf{R}'_{\theta(t)}\boldsymbol{s}_j + [\dot{\theta}(t)]^2\mathbf{R}''_{\theta(t)}\boldsymbol{s}_j, \quad (j = 1,\ldots,N) \tag{17}$$

where $\boldsymbol{s}_j$ is the X_t–Y_t position of the jth cabinet's centroid. The largest peak total acceleration experienced by any of the cabinets is given by

$$a_{\max}^t = \max_{j \in \{1,\ldots,N\}} \max_t \left\| \boldsymbol{a}_j^t(t) \right\| \tag{18}$$

The allowable limit on $a_{\max}^t$ is taken to be $0.3g$ [38], which if exceeded constitutes a failure of the isolation system to perform adequately.

Even though the bowl parameterization (13) effectively governs the accelerations sustained by the equipment, RISs are prone to failure because of excessive relative displacements resulting in impacts with the bowl lip resulting in acceleration spikes [20]. While this limit state will be captured by the response quantity $a_{\max}^t$, the relative displacement across the bearings also serves as a response quantity of interest. The largest peak relative bearing deflection is given by

$$d_{\max} = \max_{i \in \{1,\ldots,n\}} \max_t \left\| \boldsymbol{p}_i(t) \right\| \tag{19}$$

The allowable limit on $d_{\max}$ is taken to be 18 cm (twice the bowl radius r_o), beyond which an impact occurs degrading the system's performance.

The third engineering demand parameter is the peak rotation

$$\theta_{\max} = \max_t |\theta(t)| \tag{20}$$

18
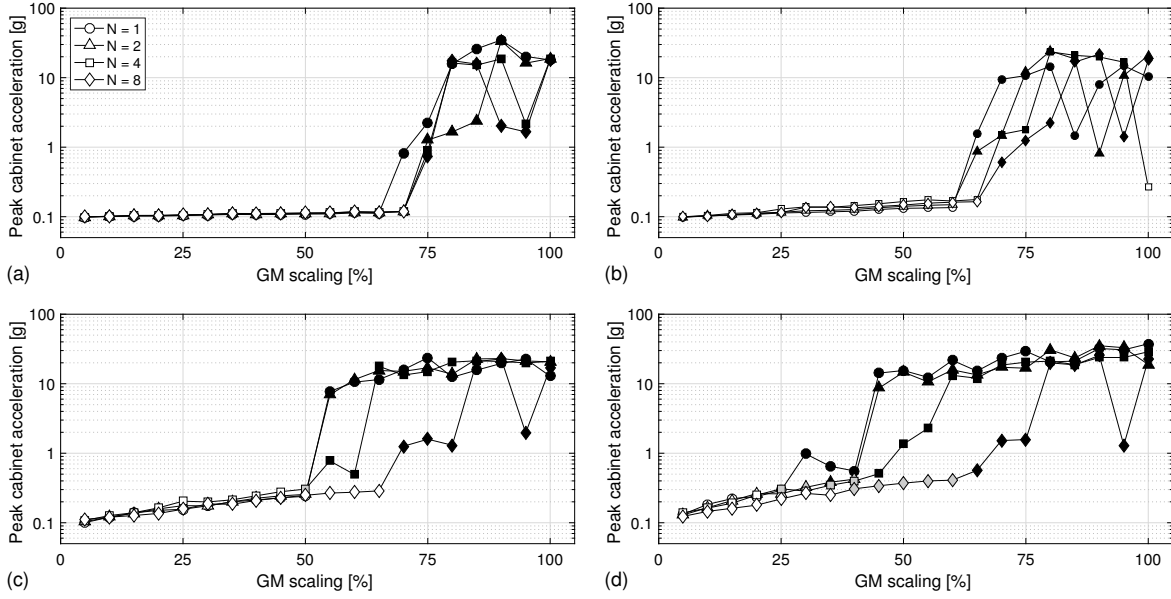
Figure 12: IDA curve of peak acceleration a_{max}^t of isolated cabinets in the side-to-side orientation with eccentricity e_y = (a) 0, (b) 12, (c) 24, and (d) 36 cm, indicating responses with (I) $a_{max}^t \leq 0.3g$ (white); (II) $a_{max}^t > 0.3g$, $d_{max} < 18$ cm (grey); and (III) $a_{max}^t > 0.3g$, $d_{max} \geq 18$ cm (black).

As observed in the forced response results (Section 3.3), an eccentric mass introduces rotations into the response which may lead to impacts in a bearing. Additionally, rotations have the effect of influencing the sustained accelerations due to centripetal acceleration [see Eq. (17)]

Figs. 12, 13, and 14 show the IDA curves for the three engineering demand parameters: a_{max}^t, d_{max}, and θ_{max}, respectively. The markers are color coded to indicate three distinct types of response: (I) $a_{max}^t \leq 0.3g$; (II) $a_{max}^t > 0.3g$ without impact; and (III) $a_{max}^t > 0.3g$ with impact. Response type I is desirable in terms of isolation performance as the equipment will remain operational, while types II and III constitute failures. Type III corresponds to the bearing capacity being reached ($d_{max} \geq 18$ cm) and impacts with the bearing lip/edge occurring; these failures are accompanied by large spikes in acceleration. The sensitivity of each demand parameters to variation in number of cabinets and mass eccentricity is discussed in the following sections.

4.2. Peak acceleration

Fig. 12 shows the IDA curve of peak acceleration a_{max}^t. Without mass eccentricity (Fig. 12(a)0, the peak acceleration is nearly constant for all cases due to the constant slope of the rolling bearing up till a GM scaling of 70% (65% for $N = 1$ discussed later). Beyond 70%, a distinct "breaking point" occurs when the peak displacements reach the 18-cm limit producing impacts within the bearings causing excessive spikes

19

in acceleration. With mass eccentricity (Figs. 12(b–d)), the peak acceleration gradually increases with GM scaling, which is due to rotations induced by an eccentric center of mass. This effect is increased with larger eccentricities. For e_y = 24 and 36 cm (Figs. 12(c,d)0, excessive accelerations are observed in the absence of an impact (response type II) due to centripetal accelerations. The eccentricity also has an effect on the breaking point at which impacts occur for a given number of cabinets, decreasing the GM scaling required for impact.

The number of cabinets has little effect on the peak acceleration when there is no eccentricity (Fig. 12(a)); the single cabinet setup (N = 1) does hits the breaking point at 65% versus the ganged cabinet setups which occur at 70%. This is due to the single cabinet setup not having a middle plank that carries twice the load, resulting in less damping overall. The effect of the number of cabinets is more pronounced in the presence of a mass eccentricity (Figs. 12(c–d)). Systems with a greater number of cabinets exhibit slightly smaller accelerations. This is because the mass moment of inertia increases quadratically with N, with no change in eccentricity, resulting in a greater resistance to rotation and lower centripetal accelerations. Additionally, the distance through which the gravitational restoring forces act is larger, providing greater moment resistance. As a result, for a given mass eccentricity, the critical GM scaling at which impacts occur is higher for greater number of cabinets.

4.3. Peak bearing displacement

Fig. 13 shows the IDA curve of peak bearing displacement d_{max}. The peak displacement increases with increasing GM scaling until a bearing displacement of 18 cm is reached, beyond which d_{max} is stunted due to impacts with the bowl lip. Peak bearing displacements beyond the theoretical limit of 18 cm are predicted by the model for the cases in which impacts occur. As previously discussed, the numerical model does not rigorously model impacts, but instead a very stiff region is included in the assumed bowl profile [Eq. (13)] to simulate impacts. While the predicted excessive bearing displacements are not observed experimentally at impact, there is a transition of energy from the isolation mode to the structural mode of the cabinet. Though the model treats the isolated cabinets as rigid, these predicted displacements may be interpreted as body deformations in the isolated cabinet or rocking of the cabinet. With that said, the quantitative accuracy of these predictions are suspect, but may be improved through a fitting of the secondary slope s_o in the bowl geometry [Eq. (13)], which is a topic of ongoing research.

The peak bearing displacements are quite sensitive to the level of eccentricity within the cabinets. With larger eccentricity comes larger rotations, which in turn lead to larger bearing displacements (without larger
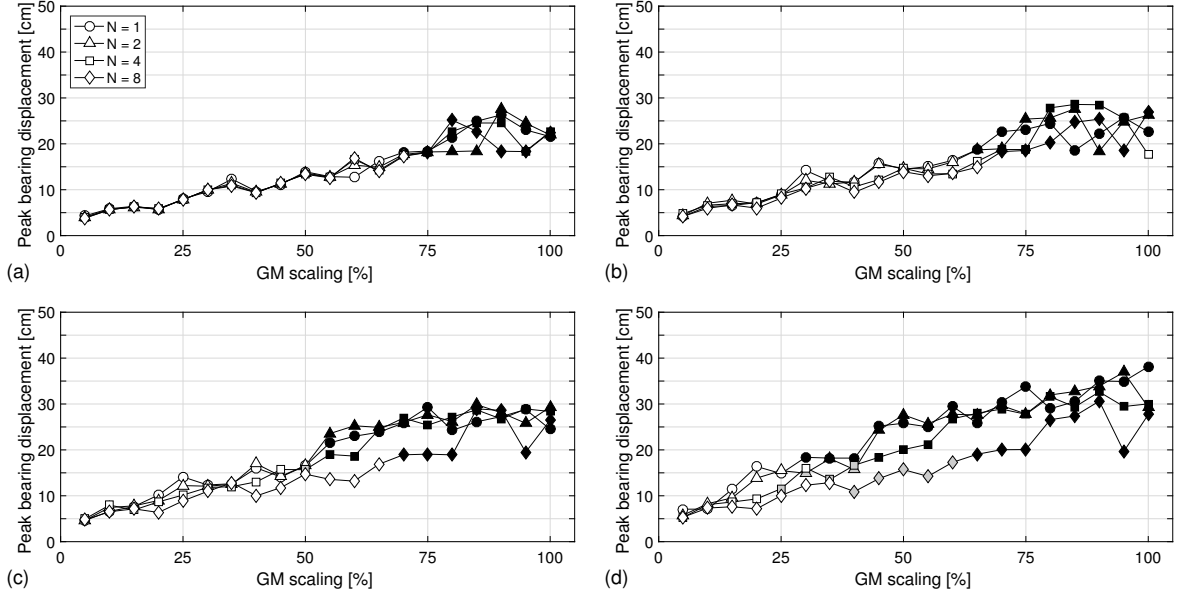
Figure 13: IDA curve of peak bearing displacement d_{max} of isolated cabinets in the side-to-side orientation with eccentricity $e_y =$ (a) 0, (b) 12, (c) 24, and (d) 36 cm, indicating responses with (I) $a_{max}^t \leq 0.3g$ (white); (II) $a_{max}^t > 0.3g$, $d_{max} < 18$ cm (grey); and (III) $a_{max}^t > 0.3g$, $d_{max} \geq 18$ cm (black).

centroidal displacements). Impacts are therefore reached at lower GM scales as the eccentricity increases. Higher peak displacements are also seen for fewer cabinets ($N = 1, 2$) than for higher number of cabinet ($N = 4, 8$) for all GM scalings. Configurations with more cabinets are better able to resist rotations that those with fewer cabinets due to an increase in the mass moment of inertia and larger moment arm for the restoring forces.

4.4. Peak rotation

Fig. 14 shows the IDA curve of peak rotation θ_{max}. No rotations are observed for the case with zero eccentricity (Fig. 14(a)) up until impacts are predicted. Cases with eccentricity (Figs. 14(b–d)) show a roughly linear increase in θ_{max} with GM scaling up until the point of impact, at which point θ_{max} saturates to a limiting value. The theoretical maximum permissible rotation, denoted θ_o, is dictated by the geometry of the RIS platform and bearing capacity, taken to be

$$\theta_o = \arctan \frac{2r_o}{\min\{l_y, N \cdot l_x\}} \tag{21}$$

For single ($N = 1$) and ganged ($N = 2, 4$, and 8) cabinet setups, θ_o are 18.1°, 17.5°, 8.97°, and 4.51°, respectively. For zero or small eccentricity (Figs. 14(a,b)), the peak rotation abruptly jumps to the maximum
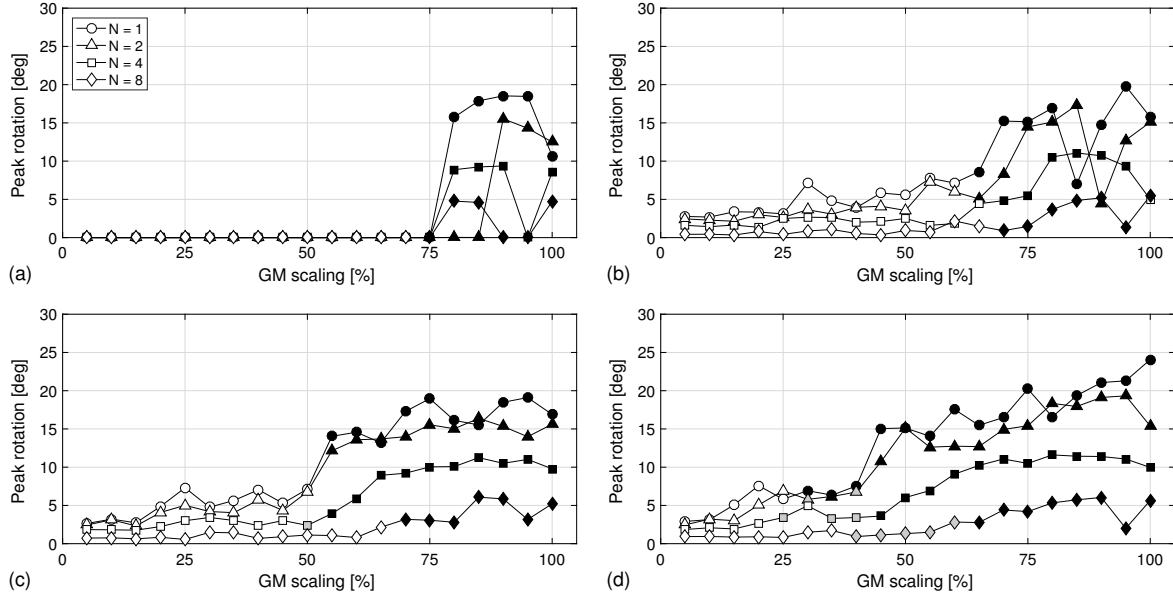
Figure 14: IDA curve of peak rotation θ_{max} of isolated cabinets in the side-to-side orientation with eccentricity e_y = (a) 0, (b) 12, (c) 24, and (d) 36 cm, indicating responses with (I) $a^t_{max} \leq 0.3g$ (white); (II) $a^t_{max} > 0.3g$, $d_{max} < 18$ cm (grey); and (III) $a^t_{max} > 0.3g$, $d_{max} \geq 18$ cm (black).

value at the "breaking point" where impacts are achieved. For these cases, the impacts occur primarily along the loading direction, and the rotations had little influence on the critical (excessive) displacement across the bearings. The resulting large rotations are due to high restoring forces produced in the elastic impact. For larger eccentricities (Figs. 14(c,d)), the peak rotation gradually increases up to the maximum value before impacts are observed. For these cases, the excessive bearing displacements leading to impact are attributed to the large rotations and accompanying bearing displacements. Because the rotations produce displacements transverse to the loading direction, the resulting impacts tend to not be along the loading direction. While the initial impact in this case can be more grazing in nature, it still produces high restoring forces inducing larger subsequent rotations and accelerations.

4.5. Performance curves

Isolation of typical building contents and nonstructural components would ideally be designed using basic charts for determining performance. From the IDA results (Figs. 12 – 14), there are distinct GM scalings at which isolation performance is degraded (i.e., the "breaking point" where impacts are observed). *Performance curves*, which depict the limiting GM scaling for which the system configurations meet the displacement capacity criteria without experiencing an impact, are shown in Fig. 15 for varying number of cabinets (a) and mass eccentricity (b). These curves give an upper bound on "acceptable performance." A
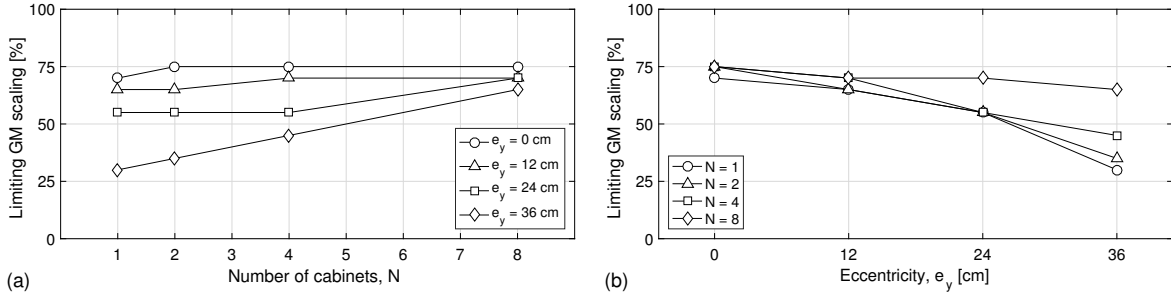
22

Figure 15: Performance curves showing the largest (limiting) ground-motion (GM) scaling without experiencing an impact for a lightly-damped RIS with varying number of cabinets and mass eccentricity: (a) constant lines for eccentricity, and (b) constant lines for number of cabinets.

higher limiting GM scaling means the system can sustain more intense shaking without an impact, indicating better performance. Fig. 15(a) shows enhanced performance with increasing number of cabinets for a constant value of eccentricity. The sensitivity of this trend increases with increasing eccentricity. Fig. 15(b) shows reduced performance with increasing eccentricity for a constant number of cabinets. The sensitivity of this trend decreases with increasing number of cabinets. A designer could use these curves to establish the required configuration (number of cabinets and eccentricity) for a given GM intensity.

5. Conclusions

In this paper, a physics-based mathematical model for the dynamics of multi-unit RIS arrays is developed. The model can be used to predict the response of RIS arrays supporting an arbitrary number of cabinets including mass eccentricity. A damping model is proposed that takes into consideration the additional load on interior planks, increasing rolling resistance modeled as viscous damping in lightly damped RISs. A linear Hooke impact model is incorporated to simulate impacts with the rolling surface edge. Predictions with the model are compared to free and forced vibration tests of actual systems with $N = 1$ and 2 isolated cabinets, showing good agreement. The model is then used to predict peak acceleration, displacement, and rotation responses with varying eccentricity, number of cabinets, ground-motion (GM) scaling, and loading direction. The limiting GM scaling at which impacts are observed was shown to be sensitive to the mass eccentricity because of the rotations induced and to number of cabinets because of the additional rotational resistance afforded by a large number of cabinets. Performance curves illustrated these sensitivities, showing that large arrays of cabinets ($N = 8$) were least vulnerable, even when large eccentricities ($e_y = 36$ cm) are present. Going forward, a more accurate impact model (e.g., Hertz type) should be explored to better capture the accelerations during impact and the responses following an impact.

23

Also, the proposed model should be validated against experimental test data considering a larger number of cabinets. The experimental results presented herein considered up to only two cabinets, but larger arrays (up to 10 cabinets) are commonly used in practice.

Acknowledgements

References

[1] M.-H. Tsai, S.-Y. Wu, K.-C. Chang, G. C. Lee, Shaking table tests of a scale bridge model with rolling-type seismic isolation bearings, Engineering Structures 29 (2007) 694–702. `doi:10.1016/j.engstruct.2006.05.025`.

[2] Y.-C. Ou, J. Song, G. C. Lee, A parametric study of seismic behabior of roller seismic isolation bearings for highway bridges, Earthquake Engineering and Structural Dynamics 39 (2010) 541–559. `doi:10.1002/eqe.958`.

[3] A. Kasalanati, A. Reinhorn, M. Constantinou, D. Sanders, Experimental study of ball-in-cone isolation system, in: Building to Last: Proceedings of the 15th Structures Congress, ASCE, New York, 1997, pp. 1191–1195.

[4] P.-Y. Lin, T.-K. Lin, Control of seismically isolated bridges by magnetorheological dampers and a rolling pendulum system, Structural Control and Health Monitoring 19 (2012) 278–294. `doi:10.1002/stc.431`.

[5] G. C. Lee, Y.-C. Ou, T. Niu, J. Song, Z. Liang, Characterization of a roller seismic isolation bearing with supplemental energy dissipation for highway bridges, Journal of Structural Engineering 136 (2010) 502–510. `doi:10.1061/(ASCE)ST.1943-541X.0000136`.

[6] T.-W. Lin, C. C. Hone, Base isolation by free rolling rods under basement, Earthquake Engineering and Structural Dynamics 22 (1993) 261–273. `doi:10.1002/eqe.4290220307`.

[7] R. S. Jangid, Stochastic seismic response of structures isolated by rolling rods, Engineering Structures 22(8) (2000) 937–946. `doi:10.1016/S0141-0296(99)00041-3`.

[8] M. Houseini, A. Soroor, Using Orthogonal Pairs of Rollers on Cancave Beds (OPRCB) as a base isolation system—part i: analytical, experimental and numerical studies of OPRCB isolators, The Structural Design of Tall and Special Buildings 20 (2011) 928–950. `doi:10.1002/tal.568`.

[9] C.-Y. Yang, C.-H. Hsieh, L.-L. Chung, H.-M. Chen, L.-Y. Wu, Effectiveness of an eccentric rolling isolation system with friction damping, Journal of Vibration and Control 18 (2011) 2149–2163. `doi:10.1177/1077546311428633`.

[10] Q. Zhou, X. Lu, Q. Wang, D. Feng, Q. Yao, Dynamic analysis on structures base-isolated by a ball system with restoring properties, Earthquake Engineering and Structural Dynamics 27 (1998) 773–791. doi:10.1002/(SICI)1096-9845(199808)27:8<773::AID-EQE749>3.0.CO;2-A.

[11] D. Foti, J. M. Kelly, Experimental analysis of a model isolated at the base with rubber-layer roller bearing (RLRB), European Earthquake Engineering 10 (1996) 3–13.

[12] I. Caliò, M. Marletta, F. Vinciprova, Seismic response of multi-storey buildings base-isolated by friction devices with restoring properties, Computers and Structures 81 (2003) 2589–2599. doi:10.1016/S0045-7949(03)00327-4.

[13] S. Cui, M. Bruneau, M. C. Constantinou, Integrated design methodology for isolated floor systems in single-degree-of-freedom structural fuse systems, Tech. Rep. MCEER-12-0004, MCEER (2012).

[14] G. Jia, I. Gidaris, A. A. Taflanidis, G. P. Mavroeidis, Reliability-based assessment/design of floor isolation systems, Engineering Structures 78 (2014) 41–56. doi:10.1016/j.engstruct.2014.07.031.

[15] A. M. Nacamuli, K. M. Sinclair, Seismic isolation: Applications of WorkSafe Technologies Ball-N-Cone Isolator, in: Structures Congress 2011, Structural Engineering Institute (SEI), Las Vegas, Nevada, United States, 2011, pp. 852–863.

[16] B.-G. Jeon, S.-J. Chang, S.-W. Kim, N.-S. Kim, Base isolation performance of a cone-type friction pendulum bearing system, Structural Engineering and Mechanics 53 (2015) 227–248. doi:10.12989/sem.2015.53.2.227.

[17] C. Chadwell, K. Brennan, M. Porter, Seismic hazard mitigation of wine barrel stacks, in: Structures 2009: Don't Mess with Structural Engineers, ASCE, 2009, pp. 1011–1019.

[18] P. S. Harvey, Jr., H. P. Gavin, The nonholonomic and chaotic nature of a rolling isolation system, Journal of Sound and Vibration 332 (2013) 3535–3551. doi:10.1016/j.jsv.2013.01.036.

[19] C. S. Tsai, Y.-C. Lin, W.-S. Chen, H. C. Su, Tri-directional shaking table tests of vibration sensitive equipment with static dynamics interchangeable-ball pendulum system, Earthquake Engineering and Engineering Vibration 9 (2010) 103–112. doi:10.1007/s11803-010-9009-4.

[20] P. S. Harvey, Jr., H. P. Gavin, Assessment of a rolling isolation system using reduced order structural models, Engineering Structures 99 (2015) 708–725. doi:10.1016/j.engstruct.2015.05.022.

[21] R. Vargas, M. Bruneau, Experimental response of buildings designed with metallic structural fuses. II, Journal of Structural Engineering 135 (2009) 394–403. doi:10.1061/(ASCE)0733-9445(2009)135:4(394).

[22] P. S. Harvey, Jr., G.-P. Zéhil, H. P. Gavin, Experimental validation of simplified models for rolling isolation systems, Earthquake Engineering and Structural Dynamics 43 (2014) 1067–1088. doi:10.1002/eqe.2387.

[23] WorkSafe Technologies, Inc., ISO-Base platform (2011).
URL http://www.worksafetech.com/

[24] D. T. Greenwood, Advanced dynamics, Cambridge University Press, New York, NY, 2003.

[25] D. Foti, A. Catalan Goni, S. Vacca, On the dynamic response of rolling base isolation systems, Structural Control and Health Monitoring 20 (2013) 639–648. doi:10.1002/stc.1538.

[26] G.-P. Zéhil, H. P. Gavin, Simplified approaches to viscoelastic rolling resistance, International Journal of Solids and Structures 50 (2013) 853–862. doi:10.1016/j.ijsolstr.2012.09.025.

[27] X. Qiu, Full two-dimensional model for rolling resistance: Hard cylinder on viscoelastic foundation of finite thickness, Journal of Engineering Mechanics 132 (2006) 1241–1251. doi:10.1061/(ASCE)0733-9399(2006)132:11(1241).

[28] P. S. Harvey, Jr., K. C. Kelly, A review of rolling-type seismic isolation: Historical development and future directions,

Engineering Structures 125 (2016) 521–531. doi:10.1016/j.engstruct.2016.07.031.

[29] S. Muthukumar, R. DesRoches, A hertz contact model with non-linear damping for pounding simulation, Earthquake Engineering & Structural Dynamics 35 (7) (2006) 811–828. doi:10.1002/eqe.557.
URL http://dx.doi.org/10.1002/eqe.557

[30] L. Guerreiro, J. Azevedo, A. H. Muhr, Seismic tests and numerical modeling of a rolling-ball isolation system, Journal of Earthquake Engineering 11(1) (2007) 49–66. doi:10.1080/13632460601123172.

[31] G.-P. Zéhil, H. P. Gavin, Three-dimensional boundary element formulation of an incompressible viscoelastic layer of finite thickness applied to the rolling resistance of a rigid sphere, International Journal of Solids and Structures 50 (2013) 833–842. doi:10.1016/j.ijsolstr.2012.11.020.

[32] N. Menga, D. Foti, G. Carbone, Viscoelastic frictional properties of rubber-layer roller bearings (rlrb) seismic isolators, Meccanica 52 (11) (2017) 2807–2817. doi:10.1007/s11012-016-0612-y.

[33] C. D. Casey, P. S. Harvey, Jr., W. Song, Seismic response of rolling isolation platforms for vibration-sensitive equipment: An experimental parametric study, Journal of Structural Engineering n/a (n/a) n/a, under review.

[34] P. S. Harvey, Jr., Vertical accelerations in rolling isolation systems: Experiments and simulations, Journal of Engineering Mechanics 142 (3) (2015) 04015091. doi:10.1061/(ASCE)EM.1943-7889.0001017.

[35] Telcordia Technologies (Ed.), Network Equipment-Building System NEBS Requirements: Physical Protection, no. GR-63-CORE, Piscataway, NJ, 2012.

[36] V. Lambrou, M. C. Constantinou, Study of seismic isolation systems for computer floors, Tech. Rep. NCEER-94-0020, National Center for Earthquake Engineering Research (1994).

[37] IBM, POWER7 Information: Vibration and Shock. Systems Hardware Information, accessed 14 April 2018 (April 2014).
URL https://www.ibm.com/support/knowledgecenter/POWER7/p7ebe/p7ebevibrationandshock.htm

[38] I. Gidaris, A. A. Taflanidis, D. Lopez-Garcia, G. P. Mavroeidis, Multi-objective risk-informed design of floor isolation systems, Earthquake Engineering & Structural Dynamics 45 (8) (2016) 1293–1313. doi:10.1002/eqe.2708.